Structural study and phase transition investigation in a simple synthesis of porous architected-ZnO nanopowder

C. Shang[1], *A. Barnabé*[*,2]

CIRIMAT — UMR CNRS 5085 Institut Carnot, Université Paul Sabatier Toulouse III, 118 route de Narbonne, 31062 Toulouse Cedex 4, France

A B S T R A C T

In this work, zinc oxide powder with a rectangular-shaped porous architecture, made of numerous spherical nanometric particles, was obtained. A simple precipitation/decomposition procedure was used comprising a zinc oxalate intermediate, obtained from zinc sulfate and oxalic acid without any additives. Detailed studies on zinc oxalate dehydration, decomposition and zinc oxide formation, were carried out using in-situ temperature X-ray diffraction and thermogravimetric analysis. During the investigation, the temperature dependence of particle sizes, lattice parameters and crystal structures of $ZnC_2O_4{\cdot}2H_2O$, ZnC_2O_4 and ZnO nanopowders were analyzed from room temperature to 450 °C. Structural transitions were also discussed. The structure and morphology of the as-prepared ZnO nanopowder were investigated by electron microscopy and compared to the crystalline rectangular shape of $ZnC_2O_4{\cdot}2H_2O$. The calcination temperature, counter ion and precipitate agent were found to be related to the product's shape and diameter. Spherical ZnO nanoparticles with diameters of less than 20 nm and a maximum specific surface of 53 m^2/g were obtained using this method.

Keywords:
Oxides
Nanostructures
Chemical synthesis
Crystal structure
Phase equilibria

1. Introduction

Zinc oxide (ZnO) has been attracting a lot of attention for its various applications, such as semi-conductor devices, photo catalysts, pigments in paints and photovoltaic uses [1–6]. The well-known properties, such as the wide direct band-gap (3.3 eV), large exciton binding energy (60 meV), low cost, environmental friendly and abundance, make it a very interesting material. For different applications, ZnO can be used in various forms and morphologies [7–13]. Syntheses of powdered form ZnO using wet chemistry methods have already been widely reported [14–20]. There are a lot of parameters during synthesis that can affect the structure and microstructure of ZnO which are essential for their performance [17–19]. Thermal decomposition of zinc oxalate has been reported to produce porous and relatively high specific surface ZnO [6] which is especially interesting for gas sensing, photovoltaic or photocatalysis applications [21,22,12]. In the particular case of dye sensitized solar cells (DSSC), ZnO was reported as a good alternative of the conventional TiO_2 semi-conductor material for the first time in 1994 [23]. Since then, a lot of works focused on the development of new DSSC nano-structured photo-anodes made of ZnO porous nanostructures with various morphologies (nanowire, nanosheet, branched-nanostructure of multi-layers material, nanowire-nanoparticle composite, …) have been reported [24,9,25–27] reaching an overall DSSC efficiency for more than 7% [28].

In the present work, the precipitation of ZnC_2O_4-based precursor in hydro-alcoholic medium was carried out first, followed by in-situ high temperature X-ray diffraction analysis of the precursor from 50 to 450 °C. Detailed structural and

* *Corresponding author*. Tel.: +33 5 61 55 77 51; fax: +33 5 61 55 61 63.
E-mail address: barnabe@chimie.ups-tlse.fr (A. Barnabé).
[1] Country of origin: China.
[2] Country of origin: France.

http://dx.doi.org/10.1016/j.matchar.2013.10.004

micro-structural studies were performed for each of the crystalline structures obtained. Finally, ZnO nanopowder with porous architecture was prepared through the obtention and thermal decomposition of zinc oxalate di-hydrate and anhydrous intermediates.

2. Experimental

2.1. Material Preparation

All the chemicals were of analytical purity grade and used as received. The raw materials used were $H_2C_2O_4{\cdot}2H_2O$ and $ZnSO_4{\cdot}7H_2O$ as sources of oxalate and zinc respectively. A solution of 0.02 mol of oxalic acid in a mixture of 192 ml of ethanol and 64 ml of water, was added dropwise into 128 ml of an equimolar solution of zinc salt in distilled water. After stirring for 1 h at room temperature, a white precipitate was obtained and separated by centrifugation and washed several times with distilled water by centrifugation again. This precipitate was dried at 80 °C for several hours to attain the $ZnC_2O_4 \cdot 2H_2O$ powder precursor. A detailed study of the thermal behavior of $ZnC_2O_4{\cdot}2H_2O$ was performed up to 450 °C, which is a temperature compromise in DSSC application between obtaining good electronic contacts and maintaining high porosity while respecting the conducting glass support stability [29]. Finally, the characteristics of the zinc oxide obtained were investigated after cooling down to room temperature.

2.2. Material Characterization

The structural and microstructural studies of the precursors and products were carried out using the following equipments and techniques. One point Brunauer–Emmett–Teller (BET) measurement was obtained with N_2 as absorption gas at 77 K by using a Micromeritics FlowSorb II 2300 apparatus. Microstructural images were produced from scanning electron microscopy (SEM) using a Field Emission Gun SEM JEOL JEM 6700F. Conventional and temperature dependent powder X-ray diffraction (XRD) analyses were performed by using Bruker D4 Endeavor and D8 Advance diffractometers respectively, both equipped with a 1D LynxEye detector (Cu Kα). For temperature dependent XRD, the sample was heated in an Anton Paar HTK 1200 N heating chamber with a 30 °C/min heating rate. XRD patterns were recorded every 25 °C from room temperature to 450C° with a 20 min counting time. Rietveld refinements of the XRD patterns were performed using the FullProf/Win PlotR software package, in which the background was estimated by linear interpolation, and the peak shape was modeled by a pseudo-Voigt function. The observed profile parameters extracted from the Rietveld analysis ($FWHM^{obs}$), coupled with the instrumental broadening ($FWHM^{instr}$) determined from a standard reference material (α-Al_2O_3), were used to calculate the mean crystallite apparent size (ε), by applying the Williamson–Hall plot (($FWHM^{obs} - FWHM^{instr}$)cosθ = f(sinθ)) [30]. Thermogravimetric analysis (TGA) was performed with a SETARAM DT-TGA 92B thermo-balance under air atmosphere with a heating rate of 3 °C/min.

3. Results and Discussion

Fig. 1 shows the successive characteristic evolution of the XRD patterns (2θ from 17.5° to 40°) recorded upon heating, from 50 to 450 °C for every increment of 25 °C, during the decomposition of the oxalate precursor. The corresponding TGA plot of this precursor is shown in Fig. 2. Both TGA and XRD analyses show that the zinc oxalate dihydrate precursor ($ZnC_2O_4{\cdot}2H_2O$) decomposes first to anhydrous zinc oxalate (ZnC_2O_4) at ~125 °C and then to zinc oxide (ZnO) at ~355 °C according to the following reactions:

$$ZnC_2O_4 \cdot 2H_2O(s) \rightarrow ZnC_2O_4(s) + 2H_2O(g) \quad (1)$$

$$ZnC_2O_4(s) \rightarrow ZnO(s) + CO_2(g) + CO(g). \quad (2)$$

The two experimental TGA weight losses of 18.5% and 37.8% correspond closely to the calculated values (19.0% and 38.0%) based on reactions (1) and (2).

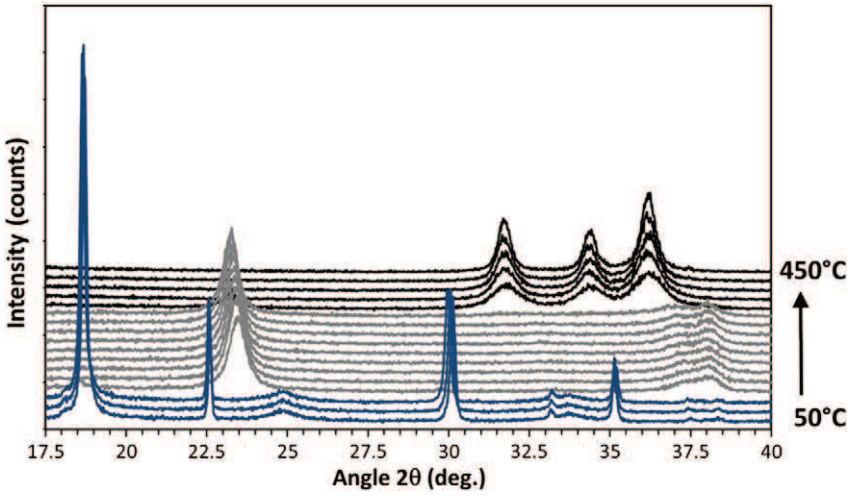

Fig. 1 – Temperature XRD patterns in the 50 to 450 °C temperature range for zinc oxalate precursor.

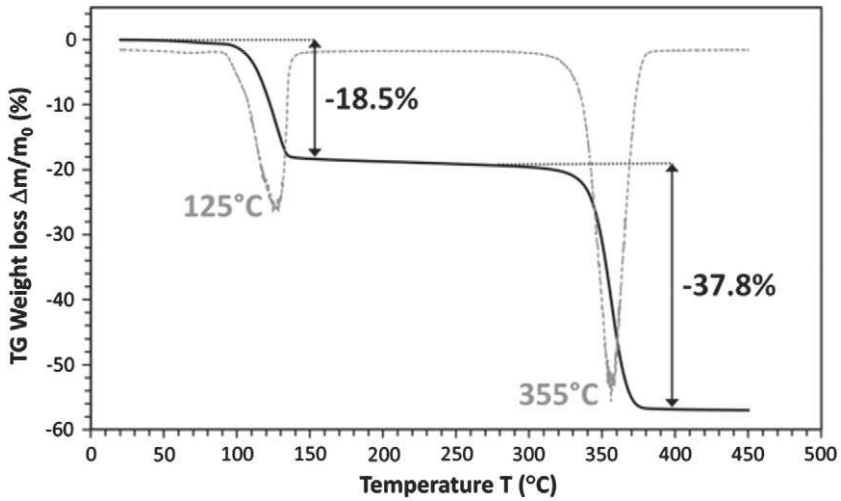

Fig. 2 – TGA/DTG curves in the 50 to 450 °C temperature range for zinc oxalate precursor.

3.1. *Zinc Oxalate Dihydrate ($ZnC_2O_4{\cdot}2H_2O$)*

At room temperature, the oxalate precursor which was directly obtained after precipitation corresponds to the pure metastable orthorhombic β form of the zinc oxalate dihydrate (β-$ZnC_2O_4{\cdot}2H_2O$). As no doublet peak located at $2\theta / \lambda_{CuK\alpha} \sim 18.74°$ is clearly visible, there is no particular reason to index the XRD pattern according to the monoclinic α form (humboldtine). This result is in good agreement with previous reports of metal oxalate dihydrate synthesized in a hydro-alcoholic solution [31,32]. The refined cell parameters determined for this zinc oxalate dihydrate phase in orthorhombic *Cccm* space group are reported in Table 1 (a_o, b_o and c_o) at 50, 75 and 100 °C. In this temperature range, the cell parameters are almost constant, the calculated X-ray density is equal to $\rho = 2.50$ g/cm^3 and the mean crystallite size is approximately $\varepsilon \sim 100$ nm. In the structure that is represented in a 3D perspective view in Fig. 3a, the zinc cation is six-folded coordinated: four oxygen anions that belong to the oxalate groups form -C_2O_4–Zn–C_2O_4–Zn- chains along the b_o axis and two apical oxygen anions that belong to the water molecules located along the a_o axis.

3.2. *Zinc Oxalate Anhydrous (ZnC_2O_4)*

At 125 °C, the dehydration induces a structure reconfiguration toward anhydrous zinc oxalate ZnC_2O_4, isostructural with β-MC_2O_4 where M = {Fe, Co, Ni, Zn, Cu, …} [33]. The refined cell parameters in monoclinic $P2_1/n$ space group (a_m, b_m, c_m and β)

Table 1 – Refined unit cell parameters, X-ray densities and mean crystallite apparent sizes of $ZnC_2O_4{\cdot}2H_2O$, ZnC_2O_4 and ZnO materials in the 50 to 450 °C temperature range.

T (°C)	Compound	Space group	a (Å)	b (Å)	c (Å)	β (°)	V (Å^3)	ρ (g/cm^3)	ε (nm)
50	$ZnC_2O_4 \cdot 2H_2O$	C ccm	11.863 (3)	5.395(1)	15.718(5)		1006.5 (8)	2.500 (2)	120
75	$ZnC_2O_4 \cdot 2H_2O$	C ccm	11.875 (2)	5.3910 (7)	15.720 (4)		1006.8 (6)	2.499 (2)	115
100	$ZnC_2O_4 \cdot 2H_2O$	C ccm	11.910 (2)	5.3886 (8)	15.734 (4)		1009.9 (6)	2.492 (2)	110
125	ZnC_2O_4	P $2_1/n$	6.042 (5)	5.24 (1)	5.253 (4)	116.0 (1)	149.5 (7)	3.41 (2)	15
150	ZnC_2O_4	P $2_1/n$	6.025 (9)	5.28 (1)	5.255 (4)	115.60 (7)	151.2 (6)	3.37 (1)	17
175	ZnC_2O_4	P $2_1/n$	6.013 (5)	5.297 (6)	5.246 (3)	115.20 (4)	151.3 (4)	3.37 (1)	17
200	ZnC_2O_4	P $2_1/n$	6.014 (6)	5.302 (7)	5.245 (3)	115.13 (4)	151.4 (4)	3.36 (1)	16
225	ZnC_2O_4	P $2_1/n$	6.016 (6)	5.294 (7)	5.241 (3)	115.21 (4)	150.9 (4)	3.37 (1)	17
250	ZnC_2O_4	P $2_1/n$	6.024 (6)	5.319 (7)	5.245 (3)	115.18 (4)	151.9 (4)	3.35 (1)	17
275	ZnC_2O_4	P $2_1/n$	6.030 (6)	5.313 (7)	5.237 (3)	115.23 (5)	151.2 (4)	3.37 (1)	17
300	ZnC_2O_4	P $2_1/n$	6.040 (6)	5.329 (6)	5.242 (3)	115.19 (4)	152.2 (4)	3.35 (1)	18
325	ZnC_2O_4	P $2_1/n$	6.051 (6)	5.337 (8)	5.249 (3)	115.13 (4)	153.3 (5)	3.32 (1)	18
350	ZnO	P $6_3/mmc$	3.253 (9)		5.22 (1)		47.8 (4)	5.65 (5)	10
375	ZnO	P $6_3/mmc$	3.257 (5)		5.223 (7)		48.0 (2)	5.63 (3)	12
400	ZnO	P $6_3/mmc$	3.259 (4)		5.217 (6)		47.9 (2)	5.64 (2)	15
425	ZnO	P $6_3/mmc$	3.259 (4)		5.222 (6)		48.0 (2)	5.63 (2)	19
450	ZnO	P $6_3/mmc$	3.260 (4)		5.223 (6)		48.1 (2)	5.62 (2)	20
50	ZnO	P $6_3/mmc$	3.250 (3)		5.209 (5)		47.6 (1)	5.67 (2)	20
50	ZnO	P $6_3/mmc$	3.250 (3)		5.209 (5)		47.6 (1)	5.67 (2)	20
450	ZnO	P $6_3/mmc$	3.260 (3)		5.222 (4)		48.0 (2)	5.62 (2)	22
50	ZnO	P $6_3/mmc$	3.250 (3)		5.209 (4)		47.6 (2)	5.67 (2)	22

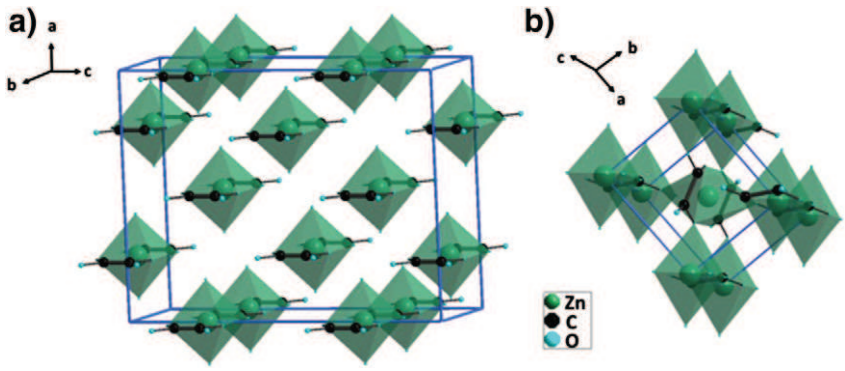

Fig. 3 – Schematic representations in perspective 3D view of the a) $ZnC_2O_4{\cdot}2H_2O$ and b) ZnC_2O_4 zinc oxalates structures.

are listed in Table 1. In this structure, every zinc atom is surrounded by six oxygen atoms, forming highly distorted octahedra which are connected to one another through corners. These six oxygen atoms all belong to oxalate groups. The first four oxygen anions are located at two similar distances from the central zinc atom ($d(Zn-O)_1$ = 1.98 Å and $d(Zn-O)_{1'}$ = 2.01 Å at 125 °C). They all form $-C_2O_4-Zn-C_2O_4-Zn-$ chains along the c_m axis (Fig. 3b). These chains with $d(Zn-Zn) = c_m$ = 5.253(4)Å in ZnC_2O_4 at 125 °C, correspond to the chains that already exist in $ZnC_2O_4{\cdot}2H_2O$, with slightly lower zinc to zinc distances ($d(Zn-Zn) = b_o$ = 5.3886(8)Å in $ZnC_2O_4{\cdot}2H_2O$ at 100 °C), due to the disappearance of the weak hydrogen bonds. The dehydration simultaneously induces a tilt of the $-C_2O_4-Zn-C_2O_4-Zn-$ chains located at x = ¼ around the b_o axis of the $ZnC_2O_4{\cdot}2H_2O$ structure. This allows one to complete the coordination of the distorted ZnO_6 octahedron in the anhydrous structure, with the two last oxygen anions located at $d(Zn–O)_2$ =2.36 Å. These two sets of d(Zn–O) are confirmed in Raman spectroscopy by characteristics peaks located at 228 and 267 cm^{-1} (Fig. 4), which are attributed to metal–oxygen stretching vibrations and are in good agreement with previous reports [34].

In the 125 to 325 °C temperature range, a_m and c_m parameters are quite stable (+0.16 and −0.08% respectively), whereas the b_m parameter significantly increases (+1.79%). The calculated X-ray density then decreases from ρ = 3.41 g/cm^3 to ρ = 3.32 g/cm^3 in this temperature range. The mean crystallite size is stable at

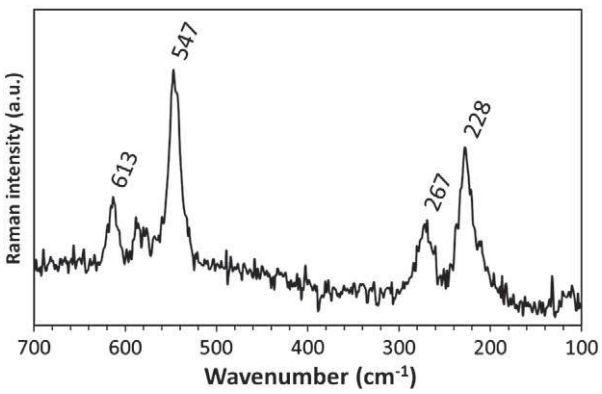

Fig. 4 – Raman spectra of the 100–700 cm^{-1} region of ZnC_2O_4.

15 < ε < 20 nm. The anisotropy of the thermal dilatation leads to an increase in the distortion of the ZnO_6 octahedron. The Zn to O bond length ($d(Zn-O)_2$), which was already large in comparison to the theoretical value ($d(Zn^{2+}{}_{VI}-O)th$ = 2.14 Å [35]), continues to increase and tends to weaken the Zn–O bond strength. At T ~ 350 °C, the structure is unstable and hence the process of structure-reconfiguration consists of the following sequence of consecutive bond breaking: the two longest Zn–O bonds, the four other Zn–O bonds, then the C–C bonds which results to the generation of a free CO_2 molecule. This pattern is in accordance with first principle calculations, performed by Kolezynski et al. [36], of band structure, density of states, electron density topology, bond orders and valences.

3.3. *Zinc Oxide (ZnO)*

Above 350 °C, pure zinc oxide with a wurtzite structure is obtained. In this structure, the zinc atoms are in tetrahedral coordination. The refined cell parameters in hexagonal $P6_3/mmc$ space group (a_h and c_h) are listed in Table 1. From 350 °C to 400 °C, as shown in Table 1, the lattice parameters vary rapidly due to the process of structure reconfiguration from the anhydrous oxalate structure to ZnO. Above 400 °C, a_h and c_h converge to reproducible values obtained for ZnO upon further cooling and heating treatments with a_h = 3.260(4)Å and c_h = 5.223(6)Å at T = 450 °C. The calculated thermal expansion coefficients α_a = 7.7 10^{-6} K^{-1} and α_c = 6.7 10^{-6} K^{-1} in the RT-450 °C temperature range defined by $\alpha_a = (1/a)(da/dT)$ or $\alpha_c = (1/c)(dc/dT)$ and the ratio, c_h/a_h = 1.60, at 450 °C are in good accordance with literature values [37]. In the 350–450 °C temperature range, while 350 °C is the lowest temperature at which ZnO could be obtained, the mean crystallite size increases from ε = 10 nm to ε = 20 nm with no crystallite shape anisotropy as previously reported by Audebrand et al. [38].

At room temperature, the lattice parameters of the so-obtained ZnO material are a_h = 3.2503(2) Å and c_h = 5.2091(3) Å with a calculated X-ray density of ρ = 5.67 g/cm^3 (Table 1). The corresponding SEM images with those of the $ZnC_2O_4.2H_2O$ precursor are presented in Fig. 5. The ZnO porous architecture, confined in a sub-micronic rectangular shape (Fig. 5b), consists of a large number of homogeneous nanometric spherical zinc oxide particles (Fig. 5c). Its specific surface, S_{BET} = 34 m^2/g, corresponds to an estimated particle size of D_{BET} = 31 nm defined by $D_{BET} = 6 \times 10^4 / \rho \times S_{BET}$ with ρ = 5.67 g/cm^3 (Table 1). This particle size is

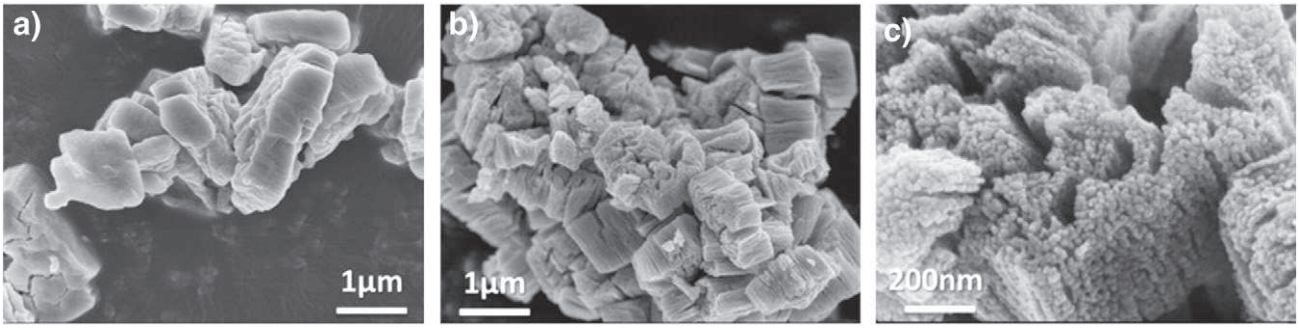

Fig. 5 – SEM micrographs of a) $ZnC_2O_4{\cdot}_2H_2O$, b) ZnC_2O_4 and c) Zn_O.

consistent with XRD and SEM measurements with D_{XRD} = 27 nm (D_{XRD} = 4/3 ε because the particles are spherical) and D_{SEM} = 20–40 nm respectively.

The particle size of the ZnO nanopowder in this porous architecture is temperature dependent due to the merging of the smaller particles into larger ones through solid state diffusion [39]. For ZnO prepared by the same process but decomposed only at 350 °C, the particle size is approximately 50% smaller than that of 450 °C with D_{BET} = 20 nm (S_{BET} = 53 m^2/g) and D_{XRD} = 13 nm, whereas at 500 °C, the particle size increases up to D_{XRD} = 48 nm. The particle size of the ZnO nanopowder in this porous architecture is also counter ion dependent. With the same synthesizing process by using nitrate ($Zn(NO_3)_2$) instead of sulfate as the zinc source. The ZnO particle size obtained at 450 °C is D_{BET} = 71 nm, i.e. twice of that from the $ZnSO_4$ precursor. This has also been corroborated by Raj et al., in which ZnO nanopowder with similar architecture but larger crystalline and particle sizes were obtained from zinc chloride salt and oxalic acid at 500 °C.

This porous ZnO architecture is precursor dependent as demonstrated by the SEM in Fig. 5a. The micrograph of the oxalate precursor exhibits an identical rectangular shape. During the calcination process, the initial pore in the precursor is formed by the release of the two water molecules (Reaction (1)). Hence, the pore volume further increased for T ≥ 350 °C with the subsequent release of CO_2 and CO from the precursor (Reaction (2)), the simultaneous nucleation and growth of ZnO primary particles. This is in good agreement with the work of Jia et al. [11].

4. Conclusion

ZnO nanopowders with porous architecture were synthesized by a simple and inexpensive method. This method consists of 1) precipitation of metastable orthorhombic zinc oxalate dihydrate (β-$ZnC_2O_4{\cdot}2H_2O$) in a hydro alcoholic solution from zinc salt and oxalic acid at room temperature, 2) its dehydration into monoclinic anhydrous zinc oxalate (β-ZnC_2O_4) at 125 °C and 3) decomposition into zinc oxide nanopowder at 350 °C. Detailed crystalline parameters for each of the species were analyzed and the phase transition mechanisms between different structures were shown in detail by high temperature XRD coupled with TGA analysis in the temperature range of RT-450 °C. From the XRD, SEM and BET analysis, it was confirmed that the resultant ZnO porous architecture consists of a large number of homogeneous nanometric spherical zinc oxide particles with a pure hexagonal wurtzite structure, confined in a sub-micronic rectangular shape. The particle size of the ZnO nanopowder has been proven to be temperature and counter ion dependent. In this synthesis, ~13 to 20 nm spherical ZnO particles with a 53 m^2/g specific surface could be easily obtained, rendering it a very interesting candidate as a photo catalyst and for photovoltaic application.

Acknowledgments

The equipment support for temperature XRD from Fédération de Recherche FERMAT is gratefully appreciated. CS thanks the PRES-Région Midi-Pyrénées for the financial support.

REFERENCES

[1] Pan Z, Dai Z, Wang Z. Nanobelts of semiconducting oxides. Science 2001;291:1947–9.
[2] Ozgur U, Alivov Y, Liu C, Teke A, Reshchikov M, Dogan S, et al. A comprehensive review of ZnO materials and devices. J Appl Phys 2005;98 [041301/1–041301/103].
[3] Li G-R, Dawa C-R, Lu X-H, Yu X-L, Tong Y-X. Use of additives in the electrodeposition of nanostructured Eu3+/ZnO films for photoluminescent devices. Langmuir 2009;25:2378–84.
[4] Yang Y, Du G, Xin X, Xu B. Hierarchical ZnO microrods: synthesis, structure, optical and photocatalytic properties. Appl Phys A Mater Sci Process 2011;104:1229–35.
[5] Sivalingam Y, Martinelli E, Catini A, Magna G, Pomarico G, Basoli F, et al. Gas-sensitive photoconductivity of porphyrin-functionalized ZnO nanorods. J Phys Chem C 2012;116:9151–7.
[6] Cho S, Jang J-W, Park HJ, Jung D-W, Jung A, Lee JS, et al. A method for synthesizing ZnO-carbonaceous species nanocomposites, and their conversion to quasi-single crystal mesoporous ZnO nanostructures. RSC Adv 2012;2:566–72.
[7] Lee D-K, Bang J, Park M, Lee J-H, Yang H. Organic acid-based wet etching behaviors of Ga-doped ZnO films sputter-deposited at different substrate temperatures. Thin Solid Films 2010;518:4046–51.
[8] Jimenez-Cadena G, Comini E, Ferroni M, Vomiero A, Sberveglieri G. Synthesis of different ZnO nanostructures by modified PVD process and potential use for dye-sensitized solar cells. Mater Chem Phys 2010;124:694–8.

[9] Umar A, Al-Hajry A, Hahn YB, Kim DH. Rapid synthesis and dye-sensitized solar cell applications of hexagonal-shaped ZnO nanorods. Electrochim Acta 2009;54:5358–62.
[10] Ke L, Bin Dolmanan S, Shen L, Pallathadk PK, Zhang Z, Lai DMY, et al. Degradation mechanism of ZnO-based dye-sensitized solar cells. Sol Energy Mater Sol Cells 2010;94:323–6.
[11] Jia Z, Ren D, Xu L, Zhu R. Preparation, characterization and photocatalytic activity of porous zinc oxide superstructure. Mater Sci Semicond Process 2012;15:270–6.
[12] Xie D, Chang L, Wang F, Du G, Xu B. Ultrasound-assisted synthesis of macro-/mesoporous ZnO double-pyramids and their optical and photocatalytic properties. J Alloys Compd 2012:176–81.
[13] Zheng J, Jiang Z-Y, Kuang Q, Xie Z-X, Huang R-B, Zheng L-S. Shape-controlled fabrication of porous ZnO architectures and their photocatalytic properties. J Solid State Chem 2009;182:115–21.
[14] Dhage S, Pasricha R, Ravi V. Synthesis of fine particles of ZnO at 100 degrees C. Mater Lett 2005;59:779–81.
[15] Ahmad T, Vaidya S, Sarkar N, Ghosh S, Ganguli A. Zinc oxalate nanorods: a convenient precursor to uniform nanoparticles of ZnO. Nanotechnology 2006;17:1236–40.
[16] Hu QR, Wang SL, Tang WH. Effects of alkali on the morphologies and photoluminescence properties of ZnO nanostructures. Mater Lett 2010;64:1822–4.
[17] Music S, Dragcevia D, Popovic S, Ivanda M. Precipitation of ZnO particles and their properties. Mater Lett 2005;59:2388–93.
[18] Zhu YF, Zhou GH, Ding HY, Liu AH, Lin YB, Li NL. Controllable synthesis of hierarchical ZnO nanostructures via a chemical route. Phys E 2010;42:2460–5.
[19] Hui Z, Yang D, Li S, Ma X, Ji Y, Xu J, et al. Controllable growth of ZnO nanostructures by citric acid assisted hydrothermal process. Mater Lett 2005;59:1696–700.
[20] Zareie M, Gholami A, Bahrami M, Rezaei AH, Keshavarz MH. A simple method for preparation of micro-sized ZnO flakes. Mater Lett 2013;91:255–7.
[21] Gupta SK, Joshi A, Kaur M. Development of gas sensors using ZnO nanostructures. J Chem Sci 2010;122:57–62.
[22] Dittrich T, Belaidi A, Ennaoui A. Concepts of inorganic solid-state nanostructured solar cells. Sol Energy Mater Sol Cells 2011;95:1527–36.
[23] Redmond G, Fitzmaurice D, Graetzel M. Visible light sensitization by cis–bis (thiocyanato) bis (2, 2′-bipyridyl-4, 4′-dicarboxylato) ruthenium (II) of a transparent nanocrystalline ZnO film prepared by sol–gel techniques. Chem Mater 1994;6:686–91.
[24] Jimenez-Cadena G, Comini E, Ferroni M, Vomiero A, Sberveglieri G. Synthesis of different ZnO nanostructures by modified PVD process and potential use for dye-sensitized solar cells. Mater Chem Phys 2010;124:694–8.
[25] Mou J, Zhang W, Fan J, Deng H, Chen W. Facile synthesis of ZnO nanobullets/nanoflakes and their applications to dye-sensitized solar cells. J Alloys Compd 2011;509:961–5.
[26] Lu L, Li R, Fan K, Peng T. Effects of annealing conditions on the photoelectrochemical properties of dye-sensitized solar cells made with ZnO nanoparticles. Sol Energy 2010;84:844–53.
[27] Lee CH, Chiu WH, Lee KM, Yen WH, Lin HF, Hsieh WF, et al. The influence of tetrapod-like ZnO morphology and electrolytes on energy conversion efficiency of dye-sensitized solar cells. Electrochim Acta 2010;55:8422–9.
[28] Chen LY, Yin YT. Hierarchically assembled ZnO nanoparticles on high diffusion coefficient ZnO nanowire arrays for high efficiency dye-sensitized solar cells. Nanoscale 2013;5:1777–80.
[29] Hagfeldt A, Gratzel M. Chem Rev 1995;95:49–68.
[30] Langford J, Louer D. Powder diffraction. Rep Prog Phys 1996;59:131–234.
[31] Lopez MC, Tirado JL, Perez Vicente C. Structural and comparative electrochemical study of M(II) oxalates, M=Mn, Fe, Co, Ni, Cu, Zn. J Power Sources 2013;227:65–71.
[32] Kanade K, Kale B, Aiyer R, Das B. Effect of solvents on the synthesis of nano-size zinc oxide and its properties. Mater Res Bull 2006;41:590–600.
[33] Kondrashev Y, Bogdanov V, Golubev S, Pron G. Crystal structure of the ordered phase of zinc oxalate and the structure of anhydrous Fe^{2+}, Co^{2+}, Ni^{2+}, Cu^{2+} oxalates. J Struct Chem 1985;26:74–7.
[34] Raj CJ, Joshi RK, Varma KBR. Synthesis from zinc oxalate, growth mechanism and optical properties of ZnO nano/micro structures. Cryst Res Technol 2011;46:1181–8.
[35] Shannon R. Revised effective ionic radii and systematic studies of interatomic distances in halides and chalcogenides. Acta Crystallogr A 1976;32:751–67.
[36] Kolezynski A, Malecki A. First principles studies of thermal decomposition of anhydrous zinc oxalate. J Therm Anal Calorim 2009;96:645–51.
[37] Iwanaga H, Kunishige A, Takeuchi S. Anisotropic thermal expansion in wurtzite-type crystals. J Mater Sci 2000;35:2451–4.
[38] Audebrand N, Auffrédic J-P, Louër D. X-ray diffraction study of the early stages of the growth of nanoscale zinc oxide crystallites obtained from thermal decomposition of four precursors. General concepts on precursor-dependent microstructural properties. Chem Mater 1998;10:2450–61.
[39] Singh P, Kumar A, Kaushal A, Kaur D, Pandey A, Goyal RN. In situ high temperature XRD studies of ZnO nanopowder prepared via cost effective ultrasonic mist chemical vapour deposition. Bull Mater Sci 2008;31:573–7.